

ELECTROKINETICS MODELS FOR MICRO AND NANO FLUIDIC IMPEDANCE SENSORS

Yi Wang*, Hongjun Song, Ketan Bhatt, Kapil Pant
CFD Research Corporation
Huntsville, Alabama 35805

Monserrate C. Roman
NASA Marshall Space Flight Center
Huntsville, AL 35812

Eric Webster, William Diffey, Paul Ashley
US Army RDECOM
Redstone Arsenal, Redstone Arsenal, Alabama, 35898

ABSTRACT

Microfluidics- and nanofluidics-based impedance sensors play an important role in identification of toxic industrial chemicals and pathogens in biodetection and biodefense arena. However, their efficient modeling and design continues to be a challenge. This paper presents high-fidelity models to resolve the electrokinetic transport process at the micro- and nano-scale and capture the critical effects of various design parameters on the electrokinetic transport and sensor performance such as medium concentration, electric conductivity, feature sizes, and fluidic manipulation. The models, verified by experiments, can be utilized for fast, accurate analysis, design, and protocol development of novel micro- and nano- fluidics based impedance sensors.

1. INTRODUCTION

Exposure to toxic industrial chemicals (TICs) and pathogens has been acknowledged to pose a significant risk to mission capability and warfighter health. Due to their salient fieldability, microfluidics- and nanofluidics-based impedance sensors are increasingly find favor in biodetection and biodefense arena. However, their efficient modeling and design continues to be a challenge. Analytical models describe the electric field distribution around the sense electrodes without consideration of the electrokinetic transport (Sun et al., 2007). Traditional equivalent circuit models, constructed by sets of primitive Differential-Algebraic Equations (DAEs), used to process and interpret the experimentally measured electrical impedance data (Sun and Morgan, 2010) are less useful for sensor design, in particular for nanofluidic sensors that can feature overlapped electric double layers (EDLs). Numerical analysis approaches (e.g., finite element and finite difference) have also been utilized for high-fidelity analysis, design, and interpretation of impedance sensors with the focus on a single suspension cell (Asami 2006).

In this context, this paper presents high-fidelity models to resolve the electrokinetic transport process at the micro- and nano-scale and to interrogate the sensor performance subject to the variations in design parameters

(such as medium concentration and conductivity, microchannel feature sizes, and fluidic manipulation). The models are verified by experimental data and can be used for fast, accurate analysis and design of micro- and nano-impedance sensors. The modeling framework presented in this paper and our findings can be utilized to guide sensor design and protocol development of biodetection technologies and also to interpret the experimental data/observations for technological refinement. The paper is organized as follows. The impedance sensor design, computational models and methods will be first described in Section 2 along with model validation and scientific findings. The analysis of pathogen impedance sensor will be presented in Section 3. The paper concludes with a summary in Section 4.

2. MOLECULAR IMPEDANCE SENSORS

2.1 Sensor Design

Figure 1 illustrates the principle of impedance-based molecular detection. The solution containing the analytes of interest is introduced into a microfluidic or nanofluidic environment (see Figure 1a). A pair of electrodes is energized with an AC field (characterized by a voltage and frequency). The induced current is related to the applied voltage and impedance of the system, which in turn is dependent on the composition of the solution (presence or absence of target agents).

In an analogy to electrical circuit theory, we can consider impedance in the solution as a combination of resistance and capacitance, with the solution acting as a resistor (R_{sol}), while the Electric Double Layer (EDL) at the electrode surface and the solution in the channel acting as capacitors (C_{DL} and C_{sol}). The equivalent electrical circuit and resistor-capacity connection is illustrated in Figure 1c. The concentrations of analytes and electrolytes impact the impedance in two ways: (1) Resistivity (or resistance) of the solution is a function of its electrical conductivity and, hence, depends on electrolyte and analyte concentrations; (2) EDL capacitance is a function of double layer thickness (which in turn is a function of electrolyte concentration) and

Report Documentation Page				Form Approved OMB No. 0704-0188	
Public reporting burden for the collection of information is estimated to average 1 hour per response, including the time for reviewing instructions, searching existing data sources, gathering and maintaining the data needed, and completing and reviewing the collection of information. Send comments regarding this burden estimate or any other aspect of this collection of information, including suggestions for reducing this burden, to Washington Headquarters Services, Directorate for Information Operations and Reports, 1215 Jefferson Davis Highway, Suite 1204, Arlington VA 22202-4302. Respondents should be aware that notwithstanding any other provision of law, no person shall be subject to a penalty for failing to comply with a collection of information if it does not display a currently valid OMB control number.					
1. REPORT DATE NOV 2010		2. REPORT TYPE		3. DATES COVERED 00-00-2010 to 00-00-2010	
4. TITLE AND SUBTITLE Electrokinetics Models for Micro and Nano Fluidic Impedance Sensors				5a. CONTRACT NUMBER	
				5b. GRANT NUMBER	
				5c. PROGRAM ELEMENT NUMBER	
6. AUTHOR(S)				5d. PROJECT NUMBER	
				5e. TASK NUMBER	
				5f. WORK UNIT NUMBER	
7. PERFORMING ORGANIZATION NAME(S) AND ADDRESS(ES) US Army RDECOM,Redstone Arsenal,AL,35898				8. PERFORMING ORGANIZATION REPORT NUMBER	
9. SPONSORING/MONITORING AGENCY NAME(S) AND ADDRESS(ES)				10. SPONSOR/MONITOR'S ACRONYM(S)	
				11. SPONSOR/MONITOR'S REPORT NUMBER(S)	
12. DISTRIBUTION/AVAILABILITY STATEMENT Approved for public release; distribution unlimited					
13. SUPPLEMENTARY NOTES Presented at 27th Annual Army Science Conference, Mon Nov 29th, Orlando,FL					
14. ABSTRACT Microfluidics- and nanofluidics-based impedance sensors play an important role in identification of toxic industrial chemicals and pathogens in biodetection and biodefense arena. However, their efficient modeling and design continues to be a challenge. This paper presents high-fidelity models to resolve the electrokinetic transport process at the micro- and nano-scale and capture the critical effects of various design parameters on the electrokinetic transport and sensor performance such as medium concentration, electric conductivity, feature sizes and fluidic manipulation. The models, verified by experiments, can be utilized for fast, accurate analysis design, and protocol development of novel micro- and nano- fluidics based impedance sensors.					
15. SUBJECT TERMS					
16. SECURITY CLASSIFICATION OF:			17. LIMITATION OF ABSTRACT Same as Report (SAR)	18. NUMBER OF PAGES 8	19a. NAME OF RESPONSIBLE PERSON
a. REPORT unclassified	b. ABSTRACT unclassified	c. THIS PAGE unclassified			

surface charges at the electrode. Therefore, when a sample with different ionic compositions is flowed through the system, it changes both the EDL capacitance and the solution resistance. The changes are reflected in the form of a disturbance (called “differential current”) to the induced base current.

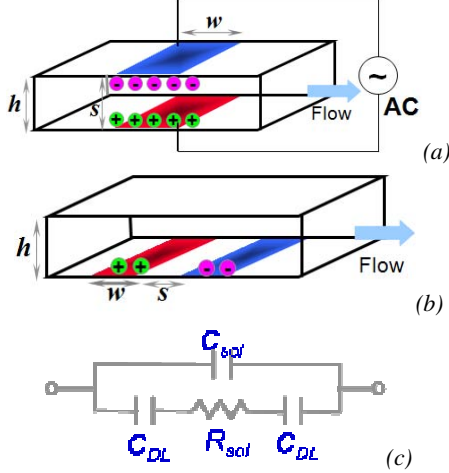


Figure 1. Principle of micro- and nano-impedance-based chemical sensors (a) Microstrip design (b) Coplanar design (c) Equivalent circuit model

2.2 Computational Models

High-fidelity, multi-physics computations are utilized to investigate the use of impedance phenomena as a basis for detection at the micro- and nano-scale. Numerical analysis was performed using CFDRC-developed multi-physics, finite volume-based simulation software, CFD-ACE+. The computational domain was meshed by a block-structured grid using the preprocessor (CFD-GEOM) available within CFD-ACE+. Two key modules – electric and chemistry – were invoked to solve the electric potential and field, and species distribution, respectively. A second-order scheme was used to calculate the ionic species distribution. The linearized algebraic equations were solved using an algebraic multi-grid (AMG) iterative method for accelerated convergence. The mathematical models are presented next.

The potential is governed by the Poisson equation

$$\epsilon_0 \epsilon_r \nabla^2 \phi + F \sum_i z_i c_i = 0 \quad (1)$$

where ϵ_0 and ϵ_r are, respectively, the electrical permittivity in the vacuum and the relative permittivity; F is the Faraday constant; z_i is the valence, and c_i is the molar concentration of the i^{th} ionic species.

The species transport in the micro- and nano-channels is described by [Wang et al., 2009]

$$\frac{\partial c_i}{\partial t} + \nabla \cdot J_i = 0 \quad (2)$$

Here the flux J_i of the i^{th} species is given by Planck-Nernst-Poisson (PNP) equation

$$J_i = -D_i \nabla c_i + u c_i + \omega_i z_i E c_i \quad (3)$$

where the terms on the R.H.S. respectively denote the species flux contributions from molecular diffusion, convection, and electromigration; ω is the electrophoretic mobility; D_i is the diffusivity; u is the velocity vector and $E = -\nabla \phi$ is the electric field. The flow of electrical current is a result of the individual flux of ions in the solution, which is given by

$$I_i = F z_i J_i = F (-z_i D_i \nabla c_i + u z_i c_i + \omega_i z_i^2 c_i E) \quad \text{and} \quad (4)$$

$$I_{\text{tot}} = \sum_i I_i = F \sum_i z_i J_i$$

The three terms on the R.H.S of the first equation in Eq. (4) signify the current contributions from diffusion, convection, and electromigration of the i^{th} ionic species, respectively.

2.3 Numerical Methods

For rapid calculation of impedance, a composite approach combining computational simulations and Fourier Transform was used. This approach harnesses the technique of potential excitation and current relaxation to extract impedance (Bessler, 2007) and, thus requires less computational effort (see Figure 2).

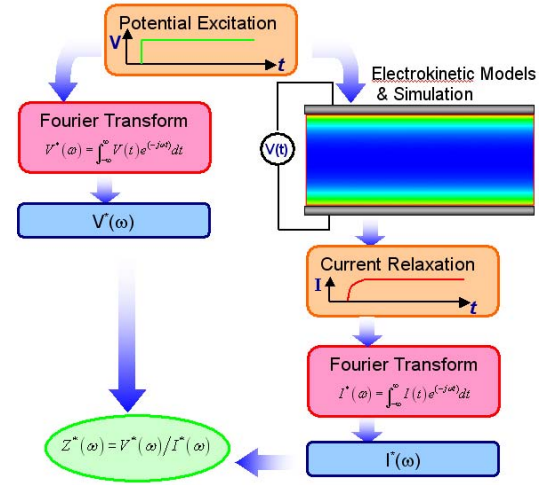


Figure 2. Computational approach for impedance calculation

Specifically, an exponential potential excitation (with time) is specified at the electrode $V(t) = \zeta + (1 - e^{(-t/\tau)}) V_{\text{step}}$, where ζ is the zeta potential of the microchannel, V_{step} the value of the step increase, and τ is the characteristic time of the potential change. Given the step potential excitation $V(t)$ at the electrodes, numerical analysis based on the electrokinetic models is undertaken to generate the current relaxation $I(t)$. The potential excitation $V(t)$ and current relaxation $I(t)$ are then transformed into the frequency domain using the Fourier Transform. The complex impedance Z^* is

$$Z^*(\omega) = Z_{\text{Re}}^* + j Z_{\text{Im}}^* = V^*(\omega) / I^*(\omega) \quad (5)$$

where ω is the angular frequency, Z_{Re}^* the real part, and Z_{Im}^* the imaginary part. As the numerical analysis

produces $I(t)$ at discrete time points t_n , viz., $I(t_n)$, a discrete version of the Fourier Transform is implemented (Bessler, 2007)

$$F^*(\omega) = \frac{j}{\omega^2} \sum_{n=1}^{N-1} \left[(-ja_n + \omega b_n + \omega a_n t_{n+1}) e^{-j\omega t_{n+1}} - (-ja_n + \omega b_n + \omega a_n t_n) e^{-j\omega t_n} \right] \quad (6)$$

Where j is the imaginary unit, $b_n = f_n - a_n t_n$, and $a_n = (f_{n+1} - f_n) / (t_{n+1} - t_n)$.

Simulations were performed to investigate three key effects to guide our choice of the sensor configuration: (1) Effect of the electrode gap (micro- vs. nano-), (2) Comparison of electrode configurations (microstrip vs. coplanar), and (3) Effect of the channel height. Relevant parameters used for these simulations are summarized in Table 1. It must be noted that given the requirement to resolve the EDL, computations involving electrode gaps larger than a few microns are prohibitively expensive. Thus, largest dimension of 5 μm (channel depth or electrode spacing) was used.

Table 1. Electrode configurations and parameters in simulations

Case	Configuration 1	Configuration 2
Micro vs. Nano	Microstrip; $h = 400 \text{ nm}$, $w = 400 \text{ nm}$	Microstrip; $h = 5 \mu\text{m}$, $w = 400 \text{ nm}$
Microstrip vs. Coplanar	Microstrip; $h = 400 \text{ nm}$, $s = 400 \text{ nm}$, $w = 400 \text{ nm}$	Coplanar; $h = 5 \mu\text{m}$, $s = 400 \text{ nm}$, $w = 400 \text{ nm}$
Effect of Channel Height	Coplanar; $h = 400 \text{ nm}$, $s = 400 \text{ nm}$, $w = 400 \text{ nm}$	Coplanar; $h = 5 \mu\text{m}$, $s = 400 \text{ nm}$, $w = 400 \text{ nm}$

The operating and property parameters for these simulations are as follows: Zeta potential (ζ) = -50 mV . Ionic strength of electrolyte (KCl) = 0.1 or 0.2 mM; $V_{\text{step}} = -5 \text{ mV}$; $\tau = 10^{-9} \text{ s}$; and frequency = $10\text{--}10^7 \text{ Hz}$. To characterize and compare the performance of the nano-impedance sensors of different configurations, three performance metrics were defined,

$$\begin{aligned} \text{Impedance:} & \quad Z \\ \text{Specific Impedance:} & \quad Z_s = ZA/s \\ \text{Impedance Sensitivity:} & \quad \alpha = \Delta Z / \Delta c \quad \text{or} \\ \text{Specific Impedance Sensitivity:} & \quad \alpha_s = \Delta Z_s / \Delta c \end{aligned} \quad (7)$$

where Z is the total impedance, which includes real $\text{Re}(Z)$ and imaginary $\text{Im}(Z)$ parts (per unit cross-sectional area of the electrodes). $\text{Re}(Z)$ represents the impedance contributed by the solution resistance, while $\text{Im}(Z)$ measures that from the capacitive effects (C_{DL} and C_{sol}). Specific impedance measures the impedance based on a unit area and unit spacing, and impedance sensitivity captures the change in specific impedance for a given concentration change.

2.4 Results and Discussion

The model was first validated by comparison against the experimental data. Following which, parametric simulations of all cases listed in Table 1 was performed to

capture the electrokinetics and ion transport in the impedance system under various sensor configurations.

2.4.1 Model Validation

Our numerical models were verified against two set of experimental data. In the first experiment, the phase angles measured from the impedance sensors using three electrode gaps (3, 7, and 12 μm in the coplanar design) with the electrolyte (KCl) concentration held constant, were compared to simulation predictions as a function of frequency observed experimentally (see Figure 3).

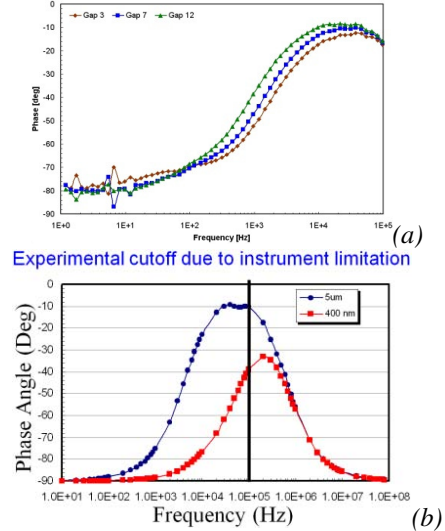


Figure 3. Phase angle for different electrode gaps in the coplanar design (a) Experiments (b) Simulations

Note that for all electrode gaps, the phase angle approaches -90° in the low and high frequency ranges and exhibits the smallest angle at the mid frequency range. This is because at the low and high frequencies, the impedance is dominated by the capacitive behavior of the EDL and bulk solution (with -90° lag between current and voltage), while in the mid frequencies, the bulk solution resistance plays the leading role (no phase lag). Another point to note is the phase angle is always smaller for larger electrode gaps due to the larger solution resistance (larger h and s) enclosed by the electrodes. A decrease in electrode gap leads to an increase in the capacitive contribution of the impedance. These results are in excellent agreement with simulation predictions, thereby validating the computational models. Due to instrument limitation, consistent experimental data for model validation could only be obtained in the frequency range below 10^5 Hz .

In the second experiment, the phase angle of impedance sensors were measured with different electrolyte (KCl) concentrations with the electrode gap kept constant (3 μm). Figure 4 shows the effect of the electrolyte concentration on the phase angle in microgap electrodes. Increase in the electrolyte concentration shifts

the impedance curve towards the high frequency. The simulation results match the experimental data very well.

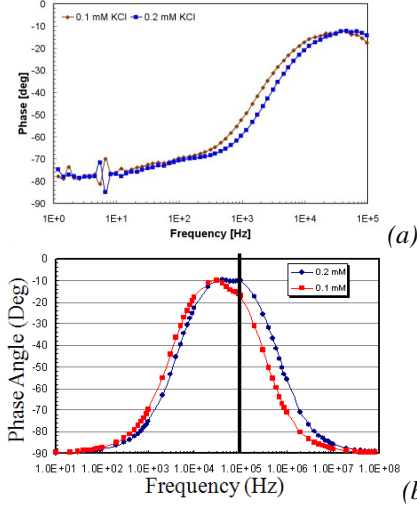


Figure 4. Phase angle for different electrolyte concentrations (a) Experiments (b) Simulations

2.4.2 Parametric Analysis

After validation, parametric numerical analysis was undertaken to evaluate the different sensor configurations.

Micro vs. Nanogap Electrodes: Two representative inter-electrode gaps of 5 μm and 400 nm were modeled to investigate the differences in micro- and nano-gap electrode impedance. The total and specific impedance spectra obtained from the simulations for 0.1 mM KCl solution is presented in Figure 5.

The total impedance spectrum (Figure 5a) can be divided into three regimes along the ascending frequency. In the low-frequency regime ($f < 10^4$ Hz for microgap electrodes), the total impedance primarily arises from the capacitance of the electric double layer (C_{DL}), which is independent of the electrode spacing. Therefore both curves coincide. In the mid-frequency range (10^4 Hz $< f < 10^6$ Hz for microgap electrodes), the impedance is dictated by the solution resistance (R_{sol}). As the microgap electrodes enclose a larger volume of electrolyte solution, larger impedance is observed in this regime, i.e., $Z \sim R_{sol} \sim h$ (or s in the microstrip configuration). In the high-frequency regime ($f > 10^6$ Hz for microgap electrodes), the capacitance due to the bulk solution (C_{sol}) dominates. In this regime, $Z \sim 1/C_{sol} \sim h$ (and s) is valid and the impedance of the microgap electrodes is higher than that of the nanogap electrodes.

From the specific impedance spectrum shown in Figure 5b, it can be seen that micro- and nano-gap electrodes differ noticeably in the low-frequency regime and begin to coincide at the medium- and high-frequency regimes. Figure 5c illustrates the specific impedance sensitivity of the sensor, in which electrolyte solution of 0.1 and 0.2 mM KCl is used, yielding $\Delta c = 0.1$ mM. The sensitivity of the nanogap impedance sensor demonstrates

significant improvement over microgap electrodes, and the regime of enhanced performance extends up to $\sim 10^5$ Hz. This observation is practically important as it confirms that the desired frequency range falls in the nominal operation.

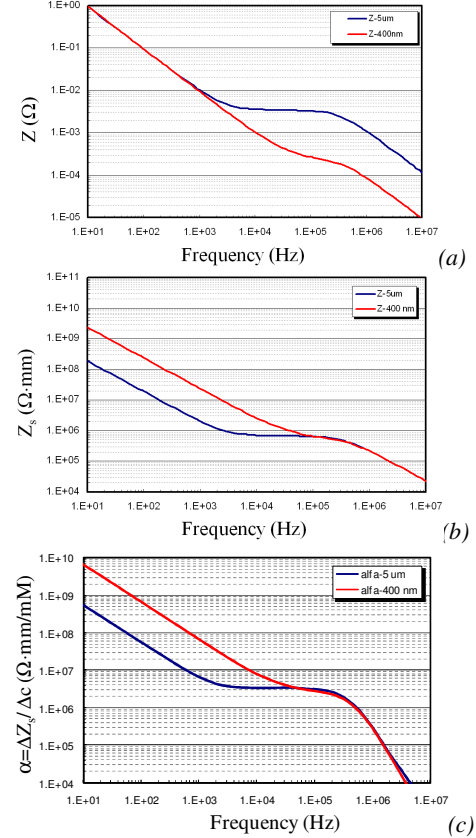


Figure 5. Effect of electrode spacing (a) Impedance, (b) Specific impedance (c) Specific impedance sensitivity

Microstrip vs. Coplanar Electrodes: Next, we investigate another key element of the impedance sensor concept, viz., microstrip vs. coplanar electrode configuration. The calculated specific impedance spectra (with 0.1 mM KCl solution) for the two configurations are shown in Figure 6a. Given the same electrode spacing, it can be seen that both coplanar and microstrip electrode configurations perform about the same. This is because in the coplanar configuration, most of the electric field lines concentrate near the gap between the two electrodes. Hence, the effective electrode spacing is essentially the same as that in the microstrip configuration. At high frequencies, impedance of coplanar configuration is larger than the microstrip, as the former encloses a larger volume of electrolyte solution (yielding larger R_{sol} and smaller C_{sol}). Figure 6b compares the sensitivity between the coplanar and microstrip design, where 0.1 and 0.2 mM KCl solution is used to calculate the specific impedance sensitivity. It can be seen that the coplanar design enables a slight improvement in sensitivity, which can be attributed to the extension of EDL area at the junction between the electrodes in the simulation.

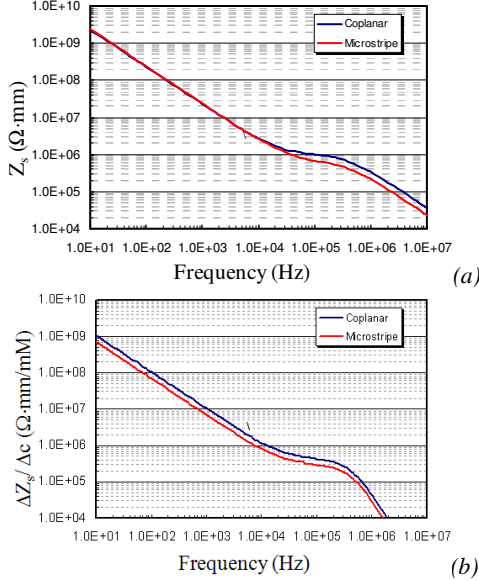


Figure 6. Microstrip vs. coplanar electrodes (a) Specific impedance (b) Impedance sensitivity

Effect of Channel Height: Based on the simulational analysis and consideration of fabrication constraints, the coplanar electrode configuration was selected for our sensor development. However, another parameter that needs to be characterized for the coplanar electrode configuration is the channel height. It is practically preferred to fabricate channels with micron-size height (e.g., 5–10 μm), without significantly compromising the sensor performance. Therefore, simulations were undertaken to evaluate the effect of channel height on sensor performance.

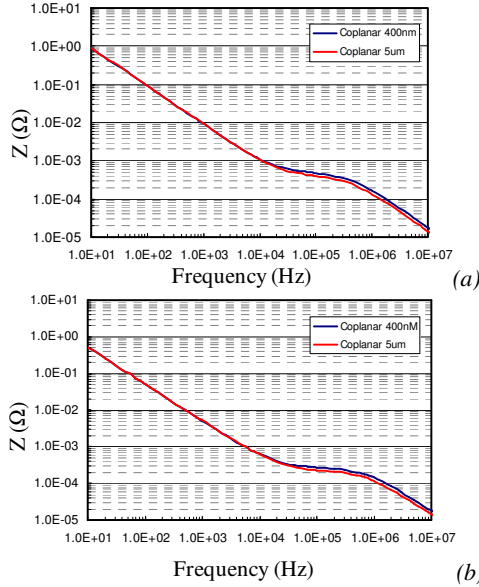


Figure 7. Effect of channel height (a) 0.1 mM KCl solution; (b) 0.2 mM KCl solution

Figure 7 shows the computed impedance spectrum of the sensor with channel heights of $h = 400 \text{ nm}$ and $5 \mu\text{m}$, both using the coplanar configuration. They are almost

indistinguishable except for a small difference at high frequencies ($>10^5 \text{ Hz}$). Therefore, it can be concluded that **increasing the channel height beyond a certain value (about the electrode gap) does not appreciably influence the electric field and impedance.**

3. PARTICULATE IMPEDANCE SENSOR

3.1 Sensor Design

We also carried out the numerical analysis and design of two types of impedance sensors that, respectively, detect the pathogenic microbes (1) suspended in solution and (2) adhered on the channel walls.

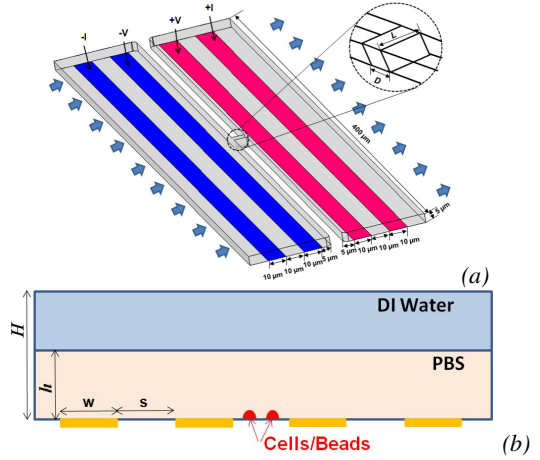


Figure 8. Impedance sensors (a) Suspended pathogen sensor and (b) Wall adhered pathogen sensor

Figure 8a shows the schematic of an impedance sensor to detect suspended microbes, which contains two bulk channels connected by a micro-pore channel (Sohn et al. 2000; Sun and Morgan, 2010). A four-probe measurement technique is used to measure the impedance changes caused by the presence of the microbe in the micro-pore. Specifically, the two outer electrodes on the bottom of the channel provide a constant excitation voltage across the sensor. When microbial cells enter the micro-pore, it displaces the suspending fluid and alters the electric impedance/resistance. The change of the impedance is microbial property-dependent and measured as the voltage ΔV or current pulse ΔI . Each cell traversing the micro-pore gives rise to a single current pulse, and hence, the number and magnitude of the pulse can be used to detect and count the microbial samples. In many cases, DC electric signal is used and the sensor reading is only due to the change in electric resistance (i.e., a microfluidic Coulter counter).

Figure 8b shows the design of an impedance sensor to detect and quantify adhered microbial cells. A conducting fluid (phosphate buffer saline or PBS) over a surface including the electrodes and captured cells/particles is pinched by a low conductivity fluid (deionized H_2O) from the top using the hydrodynamic focusing technique. A

four-electrode system is implemented wherein the impedance/resistance between the two inner electrodes can be measured as a constant current is passed between the two outer electrodes (Nasir et al., 2009).

3.2 Computational Models

All the channels in our pathogen sensor are micron-sized to facilitate the fluidic manipulation of microbes. The focus of the numerical study is to capture the effects of the sensor configurations and operating conditions; therefore the electric double layer (EDL) is not taken into account in the simulation. Thus, the electric field is governed by the AC conduction model

$$\begin{aligned} \nabla \cdot \sigma \nabla \phi_r - \nabla \cdot \omega \epsilon \nabla \phi_i &= 0 \\ \nabla \cdot \sigma \nabla \phi_i + \nabla \cdot \omega \epsilon \nabla \phi_r &= 0 \end{aligned} \quad (8)$$

where $\tilde{\phi} = \phi_r + i\phi_i$ and $\tilde{E} = \nabla \phi_r + i\nabla \phi_i$ are the complex electric potential and field. In the DC case, the imaginary parts in the above equations are absent. In addition, viscous, incompressible, fluidic model is also used in the analysis of the micro-pore sensor, which is described by the conservation of mass and momentum equations (Wang et al. 2009):

$$\frac{\partial u}{\partial t} + (u \cdot \nabla)u = \mu \nabla^2 u - \nabla p / \rho \quad \text{and} \quad \nabla \cdot u = 0 \quad (9)$$

where ρ , μ , and p are the fluid density, dynamic viscosity, and pressure respectively. CFD-ACE+ is used for the analysis. Relevant simulation parameters for the micro-pore and hydrodynamic focusing impedance sensors are summarized in Table 2 and Table 3.

Table 2. Simulation parameters for the micro-pore sensor

Chamber Width (μm)	400	Channel Height (μm)	5
Electrode width (μm)	10	Gap between electrodes (μm)	10
Channel Length L (μm)	3–9	Channel Width D (μm)	3–8
Inlet flow rate ($\mu\text{L}/\text{min}$)	0.012	Applied Voltage (V)	0.2–1
Medium Relative Permittivity	78	Cell Relative Permittivity	60
Medium Conductivity (S/m)	0.0001–0.1	Cell Conductivity (S/m)	0.01–0.03
Cell Diameter (μm)	1	Cell Length (μm)	2

Table 3. Parameters for hydrodynamic focusing sensor

PBS Conductivity (S/m)	1.5	PBS Permittivity	78
DI Water Conductivity (S/m)	5×10^{-3}	DI Water Permittivity	78
Bead Conductivity (S/m)	5×10^{-3}	Bead Permittivity	2.31
Bead Diameter (μm)	10	Bead Spacing (μm)	10
Input Current (μA)	10	Input Frequency (HZ)	20–1M
PBS Thickness h (μm)	10, 20, 50	Channel Height H (μm)	250
Electrode Width w (μm)	500	Electrode Spacing s (μm)	500

3.3 Results and Discussion

In this section, the parametric numerical analysis for the micro-pore and hydrodynamic focusing impedance sensor, and the results and findings are presented.

3.3.1 Micro-pore Sensor

For the micro-pore impedance sensor, simulations are intended to investigate two key parameters to guide device design: (1) the electric conductivity of the buffer

and (2) the micro-pore channel size. Figure 9a and Figure 9b show the simulation results of the velocity magnitude, velocity vectors and current density magnitude across the chambers and the micro-pore. As can be seen, the velocity magnitude and the current density are considerably elevated across the micro-pore. Therefore, the sensitivity of the sensor primarily relies on the resistance of the pore R_c (in the absence of the cell) and the change in resistance ΔR when the cell enters the pore. In our simulations, the normalized change in electrical resistance $\Delta R/R_c$ (i.e., sensitivity) and associated current variation ΔI are introduced to represent the sensor performance (note that the voltage changes can be obtained in a similar way).

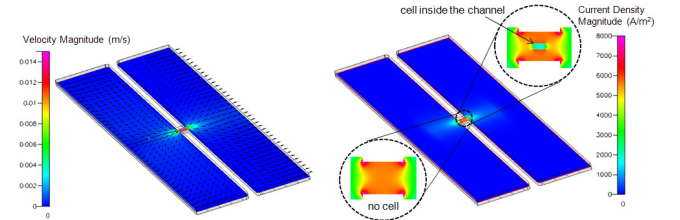


Figure 9. (a) Velocity magnitude and vectors (b) Current density magnitude across the sensor

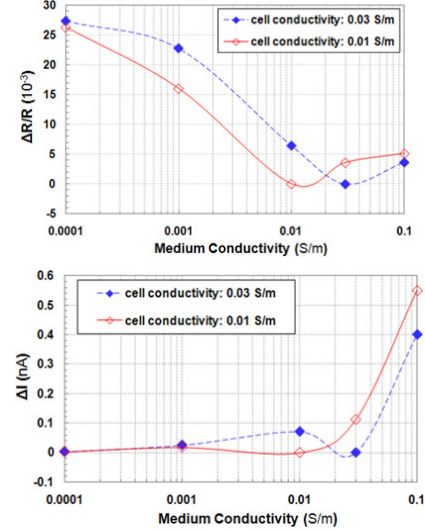


Figure 10. Effect of medium electrical conductivity (a) Normalized change in resistance $\Delta R/R_c$ (b) Current pulse ΔI

Effect of Electric Conductivity: The change in resistance under a DC electric field mainly depends on the electric conductivity of the medium and the microbial cells due to the reciprocal relationship between the resistance and electric conductivity. Simulations were carried out to analyze the changes in resistance and current in a wide range of medium conductivities (from 0.0001 to 0.1 S/m). Due to the uncertainty in its measurement, different cell conductivity (0.03 and 0.01 S/m) was used. The width and length of the pore is 5 μm and 7 μm respectively. The voltage applied between the outer electrodes is 1 V.

Figure 10a shows the normalized change in electric resistance $\Delta R/R_c$ for different medium and cell conductivities. Note that $\Delta R/R_c$ decreases rapidly to zero

when the medium conductivity approaches the value of cell conductivity. Thus, **large mismatch between the cell and medium conductivity leads to increased sensitivity of detection**, and the curve of $\Delta R/R_c$ shifts to the left when the cell conductivity decreases. Figure 10b shows that given the large resistance change, low medium conductivity (i.e., highly resistive channels) results in negligible current change ΔI , which renders the current-based detection extremely challenging. This can be addressed by either the use of high conductivity medium or voltage-based detection. Highly conductive medium is preferred to retain cell viability during the measurement, while large excitation voltage could have some deleterious effects, e.g., electrolysis at the electrodes.

Effect of the Channel Size: The length and width of the channel strongly impacts the overall channel resistance R_c and sensitivity of the sensor ($\Delta R/R_c$). A channel with a short length and a small width carries small R_c and enables high sensitivity given the same ΔR . Figure 11a illustrates the simulation results on the effects of the channel length ($L = 3, 5, 7, 9 \mu\text{m}$). Large channel length (e.g., $9 \mu\text{m}$) leads to the decreases in both $\Delta R/R_c$ and ΔI and hence, a shorter channel is desired for sensitive detection (within practical fabrication constraints). Figure 11b depicts the simulation to investigate the effect of channel width (3, 4, 5, 6, $8 \mu\text{m}$). The use of **narrow channels allows significant improvement** in both $\Delta R/R_c$ and ΔI , and hence is conducive to our impedance sensor. Therefore, channel widths needs to be appropriately selected with respect to the fabrication constraints.

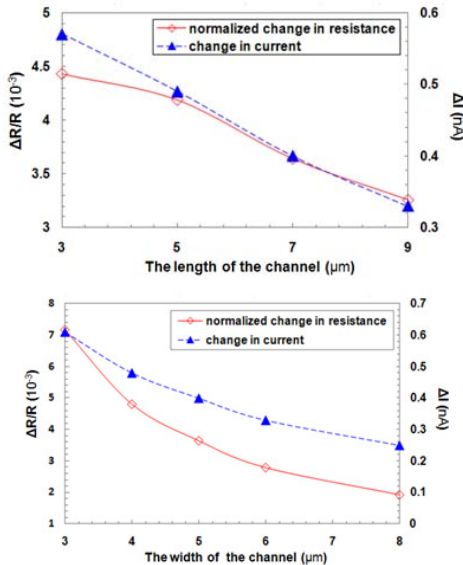


Figure 11. Effects of (a) channel length, and (b) channel width

3.3.2 Hydrodynamic Focusing Sensor

Parametric analysis were undertaken to investigate key parameters in the hydrodynamic focusing impedance sensor, including frequency, buffer thickness and number of particles. Figure 12a and Figure 12b display the

simulation results of the potential and the current density (absolute value) in the microchannel, in which the focused conductive PBS layer is $5 \mu\text{m}$ thick containing 10 particles (insulating PSL beads) between the inner electrodes. Note that most of the current flow is constrained in the conductive buffer layer. Therefore, the sensitivity and intensity of the detected signal heavily relies on the buffer thickness.

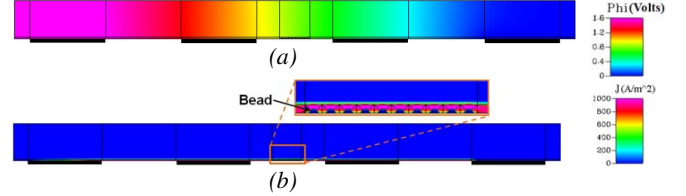


Figure 12. (a) Velocity magnitude and vectors (b) Current density magnitude across the sensor

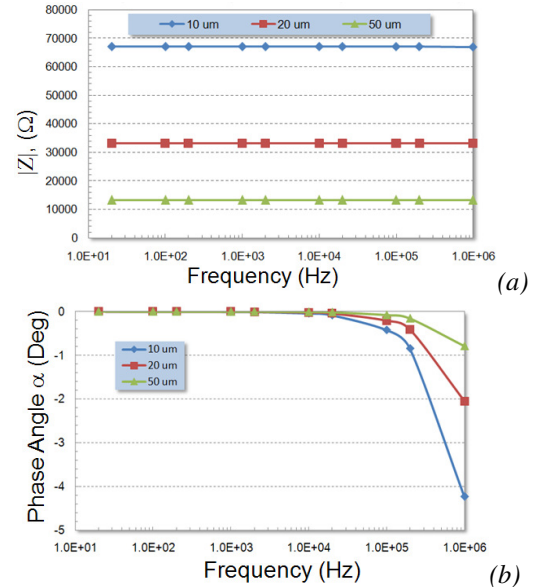


Figure 13. Effect of PBS buffer layer thickness in the frequency range (10 Hz – 1M Hz) with 10 particles

Effect of the Buffer Layer Thickness: The buffer layer thickness is the most important parameter governing the impedance sensor performance. Figure 13a illustrates the simulation results of the impedance for different buffer thickness in the given frequency range (10 Hz – 1 MHz). As the EDL effect at the electrodes is neglected in our models, the magnitude of the impedance is almost independent of the AC frequency. However, it is highly susceptible to the buffer layer thickness, and increases as the latter decreases. The phase angle is strongly dependent on AC frequency and the buffer layer thickness (see Figure 13b). The increase in the former and decrease in the latter (viz., large resistance due to small current flux area) give rise to continuously increasing displacement current through the media capacitance relative to the conduction current indicated by large phase angle and marked capacitive behavior.

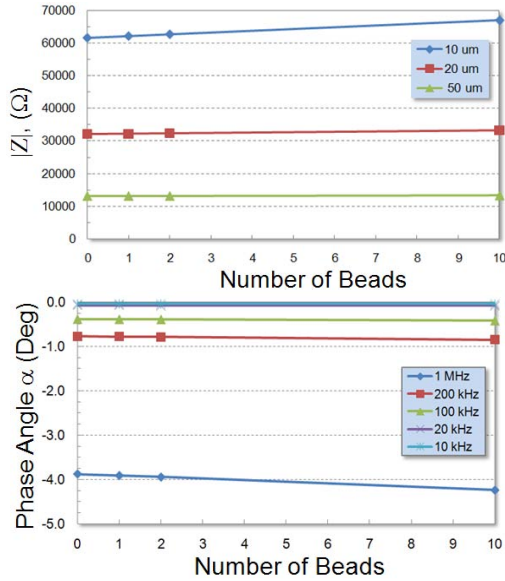


Figure 14. Effect of the number of particles (a) Impedance for different buffer layer thickness (b) Phase angle at selected frequencies

Figure 14a shows the simulation results of the impedance with different number of particles. The impedance signal grows linearly with the number of particles given a thin buffer layer (10 μm). However, a thick buffer layer (e.g., 50 μm) dilutes the impact of the number of particles on the impedance due to broadened passage for current. Therefore, **a small buffer thickness is prerequisite for detecting particle concentration with salient sensitivity.** The largest phase angle occurs at the highest frequency (1 MHz) and largest number of particles. Both scenarios increases the displacement current through the media capacitance in contrast to the conduction current, leading to a stronger capacitive behavior of the sensor and consequently, a larger phase angle. Similarly, the dependence of the phase angle on the particle number becomes negligible for a thick buffer layer.

CONCLUSION

In this paper, we investigated the electrokinetics in impedance sensors for detection of molecular and particulate targets using high-fidelity numerical models. The models were verified against experimental data. Parametric simulations, which solve the electric field, fluid flow, and species transport in a coupled manner, were performed to capture the impacts of key design parameters on sensor performance.

Specifically, for the molecular sensor, the specific impedance and sensitivity can be markedly improved by using nanochannels owing to the dimensional scaling effects. On the other hand, the electrode configuration (microstrip vs. coplanar) and the channel height in the coplanar configuration are less important for nano-impedance sensors.

For the micro-pore pathogen sensor, the electric conductivity of the medium and the pore size play a key role in the sensor design. Large mismatch between the cell and medium conductivity gives rise to the increased sensitivity. In addition, subject to the practical fabrication constraints, small pore sizes are strongly desired.

For the hydrodynamic focusing impedance sensor, a thin buffer layer is strongly entailed not only to enhance its sensitivity but also to enable its capability for beads/cells enumeration (or concentration determination). The existing model neglects the impacts of the electric double layer adjacent to the electrode, and hence, is less accurate for impedance evaluation at the low-to-middle frequency range (<10 kHz). This will be addressed in the future by including the challenging species transport model.

The above models and findings can be used not only to guide the design of impedance sensors in terms of concept down-selection, device design, and protocol development, but also to interpret experimental data and observations.

ACKNOWLEDGEMENT

This research is sponsored by the DARPA and US Army Aviation & Missile Command (AMRDEC) under contract W31P4Q-09-C-0560, and NASA/JPL under contract NNX10CE27P.

REFERENCES

- Asami, K., 2006: Dielectric dispersion in biological cells of complex geometry simulated by the three-dimensional finite difference method, *J. Phys. D: Appl. Phys.*, 39, 492-499.
- Bessler, WG., 2007: Rapid impedance modeling via potential step and current. *J. Elec.Chem.Soc.*, 154, B1186-B1191
- Nasir, M. et al., 2009: Hydrodynamic focusing of conducting fluids for conductivity-based biosensors. *Biosensor Bioelectronics*, 25, 1363-1369.
- Sohn, LL et al, 2006. Capacitance Cytometry: Measuring biological cells one by one. *PNAS*, 97, 10687-10690.
- Sun, T. et. al, 2007: Analytical electric field and sensitivity analysis for two microfluidic impedance cytometer designs, *IET Nanobiotechnol*, 1, 69-79.
- Sun, T. Morgan, H. 2010: Single-cell microfluidic impedance cytometry: a review. *Microfluidics Nanofluidics*, 8, 423-443.
- Wang, Y., Pant, K. et. al. 2009: Numerical analysis of electrokinetic transport in micro-nanofluidic interconnect preconcentrator in hydrodynamic flow, *Microfluidics Nanofluidics*, 7, 683-696